Experimental constraints on the behaviour of sulphur in the 2021 Cumbre Vieja (La Palma) basanite

Diletta Frascerra, Bruno Scaillet, Joan Andújar, Clive Oppenheimer, Stéphane Scaillet, Joan Martí, Ramón Casillas, Carmen López

Experimental constraints on the behaviour of sulphur in the 2021 Cumbre Vieja (La Palma) basanite

Diletta Frascerra[1*], Bruno Scaillet[1], Joan Andújar[1], Clive Oppenheimer[2], Stéphane Scaillet[1], Joan Martí[3], Ramón Casillas[4], Carmen López[5].

[1]Institut des Sciences de la Terre d'Orléans, UMR 7327, CNRS–Université d'Orléans–BRGM (France).
[2]Department of Geography, University of Cambridge (UK).
[3]Dep. of Geosciences, IDAEA-CSIC, Barcelona, Spain.
[4] Department of Earth Sciences, Universidad de la Laguna, Tenerife, Spain
[5] IGN, Madrid, Spain.

*Corresponding author: diletta.frascerra@univ-orleans.fr

Abstract. We performed experiments to constrain the effects of sulphur and oxygen fugacities on magma chamber and outgassing conditions of the La Palma 2021 eruption. Based on a series of controlled experiments on basanitic products carried out at 1040°C and 200 MPa, we show that sulphur addition affects the stabilities of amphibole and olivine, in particular at high fO_2 and elevated S contents which together inhibit amphibole crystallization. We also show that the overriding control on S systematics is oxygen fugacity, with melts capable of dissolving from 1000 up to 8000 ppm S, depending on fO_2. Increasing the bulk S content increases the S content of the silicate melt up to ~ 2000 ppm for fO_2<NNO+2, and 7000–8000 ppm at higher fO_2. Further increase in dissolved S is prevented by the buffering effects of either sulphide at low fO_2 or anhydrite at high fO_2. Modelling shows that the observed CO_2/SO_2 and H_2O/SO_2 ratios of volcanic gas emissions during the eruption imply a pre-existing > 5 wt% exsolved fluid in the reservoir, with fS_2 at ~ 0.1 MPa at fO_2 above NNO. Our work confirms that basaltic magmas may coexist with a significant amount of excess fluid which in turn holds an important part of the sulfur budget emitted to the atmosphere.

Keywords: La Palma, sulphur solubility, basanite, sulphur degassing

1. Introduction

The 2021 Cumbre Vieja eruption on La Palma produced ~ 0.2 km^3 of alkali basalt over a three month period, with devastating impacts on the built environment and agricultural land (Bonadonna et al., 2022; Del Fresno et al., 2023a; González et al., 2019; Ubide et al., 2023; Dayton et al., 2024). La Palma is made up of two volcanic centres. The oldest is the Taburiente centre in the north and the presently active Cumbre Vieja centre in the south of the island (Carracedo et al., 2001 and references therein). The volcanic activity of Cumbre Vieja area began about 123,000 years ago, and its complex extends from N to S being mainly composed of single eruptive centers spread along fissures. The eruptive products belong to the alkaline series, with emission of alkaline basalts, basanites, trachybasalts, tephrites and phonolites (e.g., Carracedo et al., 2001). Prior to the 2021 eruption, several eruptions have been recorded over the last 500 years (about 8), all associated with explosive events on the summit, and effusive lava flows along the flanks (Carracedo et al, 2001). La Palma is part of the oceanic island basalt system of the Canary Islands, which is fed by a hotspot of presumed mantle origin probably influenced by the rotation of the African plate (e.g., Day et al. 2022 and references therein).

The 2021 eruption was accompanied by vigorous degassing of CO_2 and S gas species, which were measured intermittently using a variety of sensors (e.g., Burton et al., 2023). Estimates of the quantity of the total SO_2 emitted range from 1 to over 4 Tg (Albertos et al., 2023; Burton et al., 2023; Dayton et al., 2024; Hayer et al., 2022). Melt inclusion analyses reveal an average pre-eruptive S content of ~ 3000 ppm (Castro and Feisel, 2022; Burton et al., 2023; Dayton et al., 2024). Complete syneruptive degassing of this sulphur would yield over 3 Tg of SO_2, i.e., an amount within the range of estimated emissions. However, estimates of initial CO_2 contents lie in the range 3–5 wt% (Burton et al., 2023), which is more than sufficient to saturate a basanite magma (e.g. Jiménez-Mejías et al., 2021; Lo Forte et al., 2024) at crustal pressures (<1 GPa). Given the likelihood of a pre-eruptive gas phase in the reservoir (Sandoval-Velasquez et al., 2023; Zanon et al., 2024; Dayton et al., 2024) raises the question of how much sulphur was partitioned into it? In silicic magmas, S is inferred to reside dominantly in the gas phase (e.g. Scaillet et al., 1998; Keppler, 1999).

Critical to understanding the behaviour of S in magmatic systems is to constrain their redox state or oxygen fugacity (fO_2), which exerts a major control on S solubility and partitioning (e.g., (Carroll and Rutherford, 1988; Luhr, 1990; Scaillet et al., 1998; Jugo, 2004; Moretti and Ottonello, 2005; O'Neill, 2021; Boulliung and Wood, 2023; Hughes et al., 2023). Knowing whether S goes into the fluid/gas or not is crucial for interpreting the composition of volcanic gases at the surface, which are routinely measured for the purposes of hazard assessment.

Our overall aim here is to develop understanding of S solubility and partitioning in mafic magmas with hotspot and ocean-island basalt (OIB) affinities through a set of experiments on La Palma 2021 basanite in which fO_2 and the amount of S were varied. To this end, we reconstructed eruptive conditions at La Palma. In particular, we focused on the amount of sulphur and its fugacity at pre-eruptive conditions in the reservoir and in the fluid phase during eruptive outgassing.

2. Experimental technique

2.1 Starting material and apparatus

Basanite lapilli (1 Top/27-9-2021) from the 2021 eruption of La Palma were selected as the starting material. The lapilli were finely ground using an agate mortar and then melted in a Pt crucible at 1400°C for 4 h at atmospheric pressure. These steps were repeated to obtain an homogeneous and anhydrous glass. Homogeneity was verified using the Electron Micro Probe analyzer (EMPA). The composition of the glass is reported in Table 1.

The experiments were performed with Internally Heated Pressure Vessels (IHPV) at the Institut des Sciences de la Terre d'Orléans (ISTO), using as pressure media either Ar or a H_2-Ar mixture gas (Scaillet et al., 1992). Up to eight gold capsules were placed in a ceramic sample holder, which was suspended between two type-S thermocouples with a Pt or Rh wire, depending on the redox conditions. During the experiments, we maintained a thermal gradient of less than 10 °C between the top and the bottom thermocouples. All experiments concluded with a rapid drop quench with cooling rates of order 100°C/s (Di Carlo et al., 2006).

SiO_2	TiO_2	Al_2O_3	FeO	MnO	MgO	CaO	Na_2O	K_2O	$P2O_5$	Cl	S	Total
44.11	3.83	14.42	12.22	0.18	7.49	10.92	4.05	1.73	0.97	0.01	0.01	97.75
(0.26)	(0.10)	(0.13)	(0.26)	(0.05)	(0.05)	(0.11)	(0.08)	(0.10)	(0.07)	(0.01)	(0.01)	

Table 1 Composition starting material

2.2 Capsule preparation and experimental conditions

The finely ground starting material was divided into three batches. Two S-bearing batches were prepared either by adding 2 wt.% native sulphur or 3 wt.% pyrrhotite (corresponding to 1.1 wt.% sulphur) and the third batch was left S-free. These bulk sulphur contents are above the sulphur solubility of basaltic melts under our experimental conditions (e.g. Moune et al. 2009; Luhr, 1990). Hence, when using the S-bearing batches directly (i.e. without mixing them with the S-free batch) as a starting material, the bulk content of sulphur should promote saturation in either sulphide or sulphate unless the coexisting fluid scavenges sulphur (see results).

For each experiment, six to seven Au capsules were prepared (inner and outer diameter of 2.5–2.9 mm, height of 1.5 cm). Gold was used to minimize the loss of sulphur and iron. Capsules were loaded first with 3 mg of deionized water to ensure fluid saturation of the system (corresponding to about 5 wt% dissolved H_2O at 200 MPa at H_2O saturation, e.g. Jiménez-Mejías et al. (2021)), then with 30 mg of silicate powder prepared by mixing S- or FeS-doped powder with S-free glass in various proportions to obtain different concentrations of sulphur (Table 2). In the following, we refer to these two series as S-doped or FeS-doped charges. The weight of the capsules was measured after welding, then after a test in an oven at 125 °C for at least 1 h, and finally after the experiment to check for volatile leaks. Only charges with a difference of less than 0.0003 g were considered successful. Considering the context of La Palma 2021 eruption as summarised above, it would have been interesting to add CO_2 as a fluid component. This however would have needed to raise the temperature of the experiments which would have in turn prohibited the use of Au containers: Containers made of either Pt or of AuPd alloys are prone to significant alteration by sulphur, which severly complicates the interpretation of results.

All the experiments were run at 1040 °C and 200 MPa but with variable fO_2 (between NNO-0.48 and NNO+4.1), controlled by sensors of NiPd for experiments above NNO and CoPd for experiments below NNO (Taylor et al., 1992; Table 2). The fS_2 of pyrrhotite-bearing charges was calculated following Froese and Gunter (1976).

On-going experiments aimed at determining pre-eruptive conditions of La Palma basalts (Andújar et al., submitted) suggest storage conditions of early erupted magmas at somewhat higher P and T (i.e., 300 MPa, 1060–1080°C). A number of petrological studies have shown that latter erupted magmas record higher pressures, >500 MPa, and temperatures above 1100°C (e.g., Castro and Feisel, 2022; Day et al., 2022; Ubide et al., 2023; Dayton et al., 2024). The reason of choice of our P-T conditions is essentially practical. As stressed above, the lower temperature allows us to use Au capsules, which considerably limits S loss from the melt+fluid towards the caspule (and also that of Fe loss), compared to either AuPd or Pt capsules, maintaining the physical integrity of containers. Such a low temperature is achieved by working with elevated melt water contents, which depress liquidus temperatures significantly in basaltic systems while maintaining the composition of near liquidus residual melts broadly basaltic (e.g., Sisson and Grove, 1993). Performing experiments at 300 MPa would have been possible, but the higher water content of the basaltic melts (>7 wt%) at this pressure renders those liquid poorly quenchable, even with drop

quench technique. Therefore, given the H_2O-reach conditions of our experiments, we decided to perform the experiments at 200 MPa, with the objective of favouring the solubility of the sulphur and facilitating the quench of the glass. Nevertheless, we recognise the potential for this approach to result in differences with the natural system, in particular a higher proportion of amphibole relative to what is observed in the rocks. Higher temperatures will also affect the solubility of sulphur: for instance an increase of 50°C in the fO_2 range NNO - NNO+1.5 increases the S solubility by 10-30%, if fS_2 is kept constant (e.g., Boulliung and Wood, 2023).

3. Analytical methods

3.1 Analytical techniques

Half of the recovered run products were embedded in epoxy and polished for optical inspection and, then carbon-coating, for scanning electron microscopy (SEM) using the Zeiss FEG of ISTO to identify phases, including those of quench origin.

Glass and minerals were analysed using a Cameca SX FIVE EMPA (CNRS-Université d'Orléans-BRGM). The analytical conditions were 15 kV, 10 nA and a peak count time of 10 s. Glasses were analysed with a defocused beam of 5, 10 or 20 µm, depending on the size of the available glass pools. Sulphur was determined using an LPET crystal and a 20 s counting time. A focused beam was used for the minerals. Sulphides were analysed during separate sessions with the following analytical conditions: 20 kV and 50 nA, using PET and LPETcrystals for S, an acquisition time of 30 s, while Fe was analyzed with LIF and LLIF crystals. The Ni and Cu had acquisition times of 10s. In addition, Si was used to detect possible glass contamination. At the beginning and end of the analytical session, two synthetic pyrrhotites of known compositions (as determined by X-ray analyses, (Clemente et al., 2004), Po5 and Po7, were analysed to check the stability of the calibration.

Three glasses with different sulphur concentrations were synthesised at 1200°C using the same experimental apparatus and starting glass. The sulphur concentrations measured by the microprobe were found to differ by less than 100 ppm relative to the added amount, validating our analytical procedure for measuring S.

The H_2O concentration in the run products was estimated following Devine et al.(1995), analyzing at the beginning and end of each analytical session standard basanitic glasses of known water contents (F1c, F05, F3c2 and F2b, in Jiménez-Mejías et al. (2021)).

3.2 Mass balance and ImageJ software calculations

The proportion of each phase was calculated by mass balance using a constrained least-squares model with the propagation of analytical errors of the experimental phases (Albarède, 1996; Scaillet and Evans, 1999). The proportion of glass was also calculated by processing SEM images at 100 µm magnification using ImageJ software, on a vesicle-free basis.

The amount of sulphur in the coexisting fluid phase was estimated by mass balance, i.e. by substracting the masses of S in sulphur-bearing phases (glass, sulphide, sulphate) from the initial mass of sulphur, taking into account the phase percentages as calculated above. The S wt% was then calculated by determining the amount of H_2O in the fluid using the same method (Table 2).

Run	P (MPa)	T (°C)	Time (min)	ΔNNO	log fO2	log fS2 (bar)	H2O&	S% and type loaded	S wt% Glass	S wt% Fluid	Mineral assemblage
lpm 1	200	1040	960	1.34	8.40	0.28	4.1	2%-native	0.22 (0.02)	9.2	Ol-Amph-Px-FeS
lpm 2						-0.24	1.8	1%-native	0.11 (0.01)	5.2	Ol-Amph-Px - Mt-FeS
lpm 33						-	4.0	0.5%-native	0.18 (0.01)	5.4	Ol -Amph - Px - Mt
lpm 4						-0.24	3.1	1.12%-FeS	0.23 (0.01)	5.1	Ol-Amph-Px-Mt-FeS
lpm 5						-	4.1	0.56%-FeS	0.21 (0.03)	6.3	Ol - Amph-Px -Mt
lpm 6						-	5.9	0.28%-FeS	0.10 (0.02)	3.5	Ol-Amph-Px-Mt
lpm 34						-	4.5	0%S	-	-	Ol-Amph-Px-Mt
lpm 7	200	1040	960	2.38	7.37	-	3.8	2%-native	0.73 (0.04)	16.6	Ol-Mt-Ilm
lpm 8						-	4.7	1%-native	0.86 (0.06)	3.6	Ol-Px-Mt
lpm 9						-	3.9	0.5%-native	0.57 (0.03)	2.5	Ol-Amph-Px-Mt
lpm 13	200	1040	360	3.30	6.44	-	5.4	2%-native	0.75 (0.04)	21.1	Ol-Mt-Ilm
lpm 14						-	6.3	1%-native	0.75 (0.04)	13.3	Ol-Px-Mt
lpm 15						-	6.8	0.5%-native	0.65 (0.09)	--	Px-Mt
lpm 16						-	2.0	1.12%-FeS	0.79 (0.03)	6.9	Px-Mt-Ilm
lpm 17						-	6.1	0.56%-FeS	0.65 (0.09)	0.3	Ol-Px-Mt
lpm 18						-	6.5	0.28%-FeS	0.33 (0.03)	1.7	Amph-Px-Mt
lpm 19	200	1040	360	4.10	5.65	-	4.8	2%-native	0.68 (0.05)	-	Ol-Px-Mt-Ilm-Anhy
lpm 20						-	5.6	1%-native	0.64 (0.01)	9.3	Ol-Amph-Px-Mt-Ilm
lpm 21						-	4.5	0.5%-native	0.58 (0.05)	3.1	Amph-Px-Mt
lpm 22						-	5.2	1.12%-FeS	0.71 (0.04)	9.0	Ol-Px-Mt
lpm 23						-	5.8	0.56%-FeS	0.65 (0.03)	3.1	Amph-Px-Mt
lpm 24						-	6.4	0.28%-FeS	0.38 (0.03)	1.4	Amph-Px-Mt-Ap
lpm 25						-	4.6	0%S	-	-	Amph-Px-Mt
lpm 26	200	1040	360	-0.48	1023	-0.63	3.5	2%-native	0.12 (0.01)	3.7	Ol-Amph-Px-FeS
lpm 27						-1.59	2.4	1%-native	0.10 (0.01)	1.2	Ol-Amph-Px-FeS
lpm 28						-	3.1	0.5%-native	0.13 (0.01)	5.5	Ol-Amph-Px-Mt
lpm 29						-1.02	3.6	1.12%-FeS	0.19 (0.03)	6.7	Ol-FeS-Mt
lpm 30						-0.75	3.1	0.56%-FeS	0.19 (0.03)	3.7	Ol-Px-FeS
lpm 32						-	4.7	0%S	-	-	Ol-Amph?-Px-Mt

Table 2 Experimental conditions, water and sulphur contents of quenched glass. H_2O is calculated with the method of Devine et al (1996). The fS_2 is calculated using the method of Froese and Gunter (1976). Amph? = quench phase

4. Results

The experiments generated different mineral assemblages, depending on fO_2 and the amount of S added, as shown in Fig. 1.

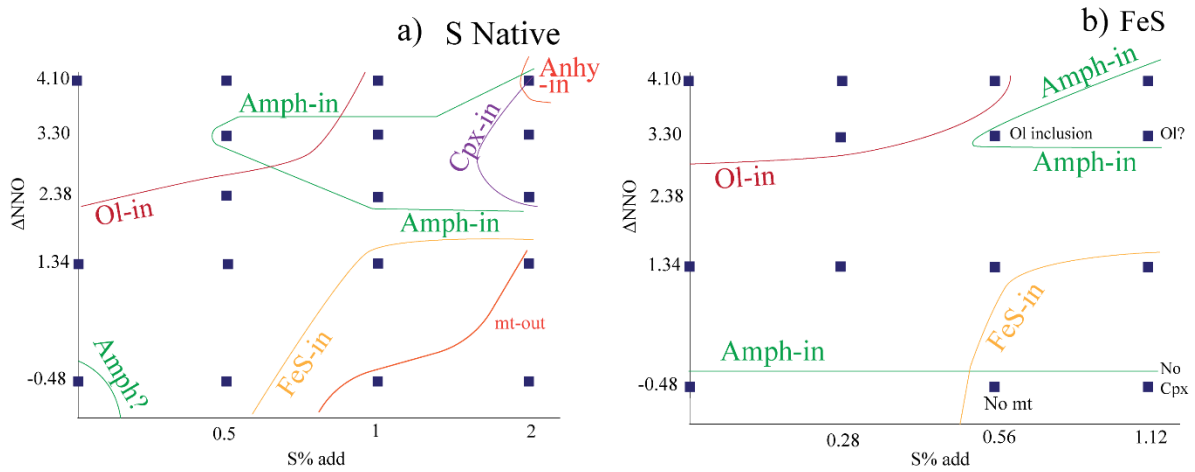

Fig. 1 Equilibrium phase diagram at 1040ºC and 200 MPa for both S-doped (a) and FeS-doped (b) charges. Phases lie inside their stability field. Ol=olivine: Cpx= clinopyroxene: Amph = amphibole; Anhy = anhydrite; mt=magnetite.

In the S-doped series, anhydrite crystallizes at high fO_2 while pyrrhotite is present at low fO_2. In detail, anhydrite is found only in the charge with 2 wt.% added S at NNO+4.1, while pyrrhotite is present with 1 wt.% and 2 wt.% S added at NNO+1.34 and NNO-0.48. Olivine occurs in almost every charge, except for those poorer in sulphur at high fO_2. Apart from three charges with 2 wt.% S added at NNO+2.38, 3.3 and 4.1, pyroxene is present in all experimental charges. Amphibole distribution is more complex. It did not crystallise in charges with 2 wt.% and 1 wt.% S at NNO+2.38, in any experiments at NNO+3.3, in the charge at 2 wt.% S under the most oxidising conditions and in the S-free charge at NNO-0.48 (Fig.1a).

The phase diagram of the FeS-doped series is broadly similar. The stability range of olivine is almost identical, except that Ol was also found in the 0.56 wt.% S charge at NNO+4.10. In the sulphur-rich experiment at NNO+3.3, Ol was not found but owing to its low abundance in other charges, it may have been overlooked. In the charge *lpm 1-top+S17*, olivine is present as inclusions in the pyroxene. Pyroxene is present in all charges, except for that with 1.12 wt.% S at NNO-0.48. FeS has a similar stability field to that identified by the S-doped series, however it is absent at 0.56 wt.% S and NNO+1.34. The amphibole field is also similar in S-doped case, except that it is not found at NNO-0.48 (Fig.1b).

188 *4.1 Major element glass and mineral composition*

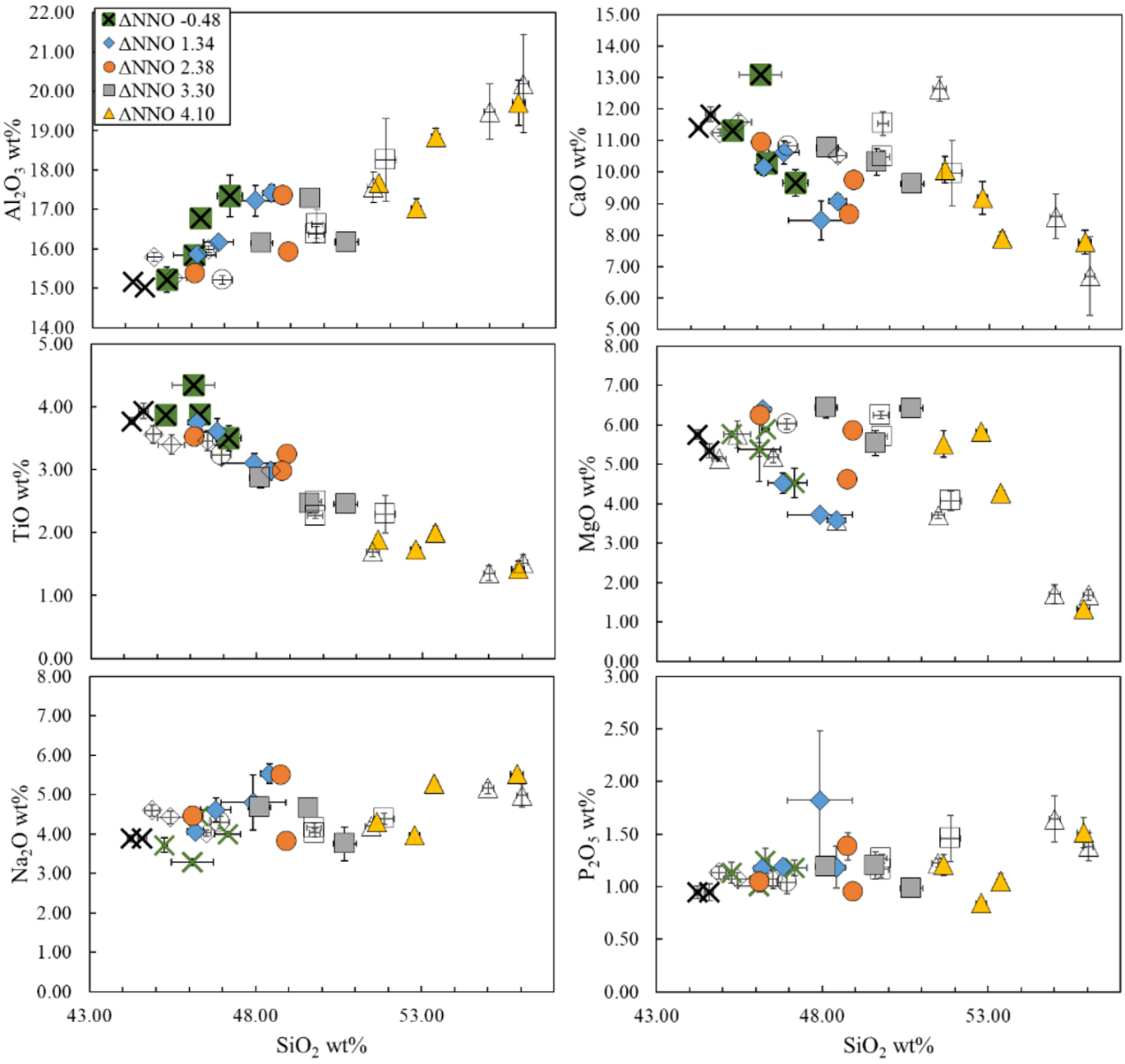

Fig. 2 Variation of oxides with SiO_2 of experimental glasses in S doped (coloured symbols) and FeS doped (open symbols) charges. When not shown, the error bars are smaller than the symbol size.

189 The major elements of glasses of both the S and FeS doped series (Table 3), show similar trends
190 (Fig. 2). SiO_2 increases regularly with fO_2, from about 44 wt.% up to a of 56 wt.%, as does Al_2O_3,
191 which reaches up to 20 wt.%, reflecting the absence of plagioclase crystallisation under the
192 investigated conditions. Reflecting clinopyroxene crystallization, CaO shows the opposite

behaviour, decreasing with increasing SiO_2 and fO_2. The same trend is observed for TiO_2 and FeO. The alkalies show no clear trends, with the possible exception of Na_2O which increased slightly with SiO_2. These fractionation trends reflect the effect of the main crystallising phases, but above all the increasing abundance of magnetite as fO_2 increases (Fig. 1).

The concentration of sulphur in the glasses does not differ between the S- or FeS-doped experiments (Fig.3). The charges produced at low fO_2 are significantly poorer in sulphur than those at high fO_2, the former having S concentration in the range 1000–2300 ppm, while the later have S

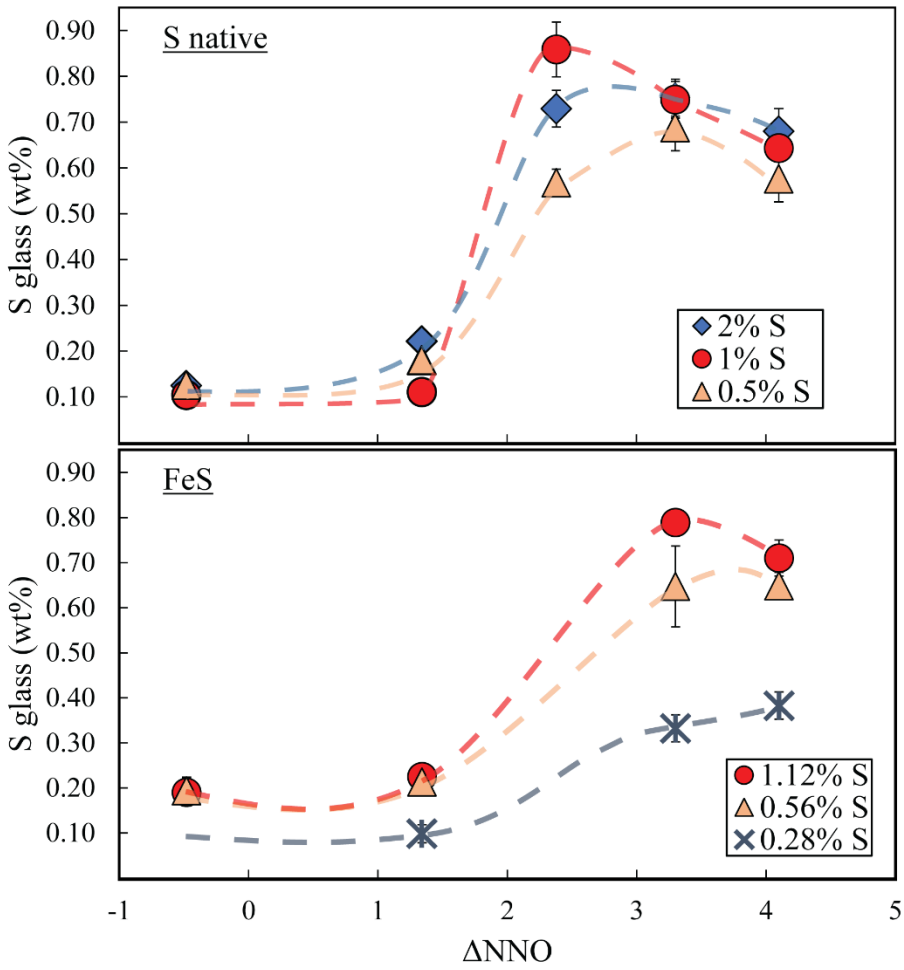

Fig. 3. Variation of S content of the glass with fO_2 as a function of wt.% of sulphur added to the capsules. When not shown, the error bars are smaller than the symbol size.

contents ranging between 3300–8800 ppm. Note however that the charge doped with 0.28 wt.% S using FeS yielded 0.8 wt.% dissolved S, which we attribute to an error in loading S to the charge. This individual run is not further considered.

From inspection of the Mg# of the glass and of Fe-Mg minerals, the amount of sulphur added does not appreciably affect their composition at fixed fO_2, though under reduced conditions

(<NNO+1.5), charges with higher bulk S contents tend to have phases with higher Mg# (in particular for charges with 2 wt.% added S). At high fO_2 the reverse is observed. Similarly, an increase in fO_2 increases slightly the Mg# of the glass and olivine, as shown in figure in Supplmentary information (SIa). No clear trends with S appears for either amphibole or pyroxene compositions (SIa).

The measured S contents in glasses saturated in pyrrhotite can be compared to those calculated using the S-solubility model of Lesne et al. (2015), which was developped for hydrous alkali-rich basalts, using the fS_2 determined by pyrrhotite (Table 2). We also calculated S contents using the model of Boulliung and Wood (2023). The results are shown in Fig. 4, illustrating a general good correspondence between calculated S contents with both models and those measured, though the Boulliung and Wood (2023) model tends to underestimate S contents. Discrepancies likely reflect analytical uncertainties in pyrrhotite composition as determined by EPMA, which translates into an uncertainty in calculated fS_2 of order ±1 log unit (e.g., Whitney, 1984). For instance, increasing log fS_2 of charge *lpm 29* from -1.02 to -0.5 (Table 2) would increase the calculated S content from

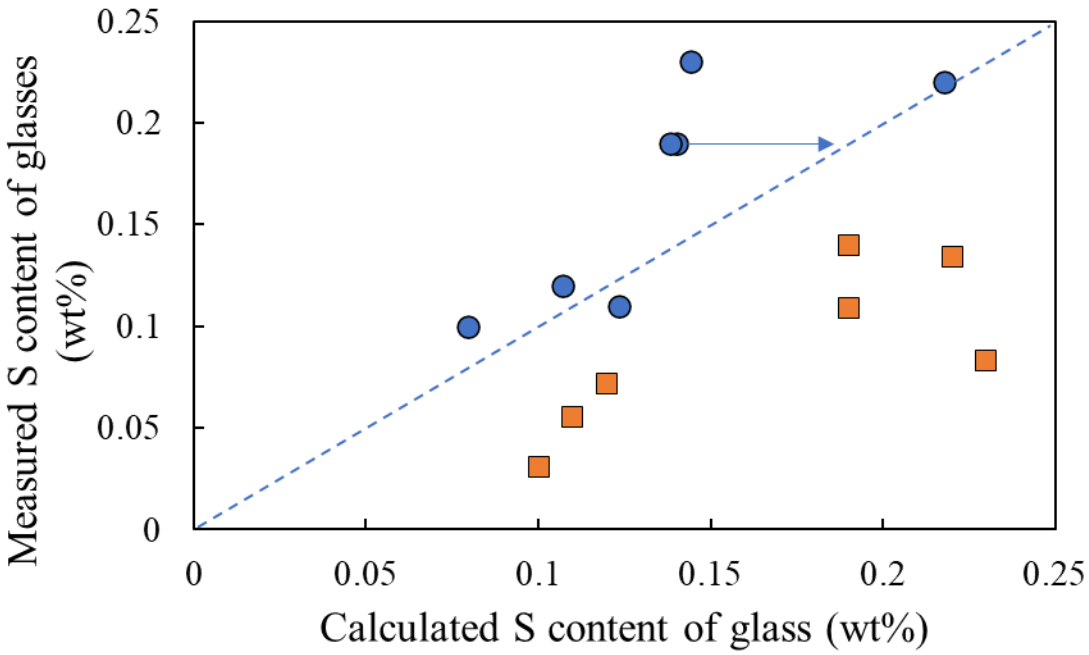

Fig. 4 Comparison between the measured S content of experimental glasses saturated in pyrrhotite with that calculated using the models of Lesne et al. (2015, blue symbols) and Boulliung and Wood (2023, orange symbols). The arrow shows the effect of increasing fS_2 by 0.5 log unit on the calculated S content of melt with the model of Lesne et al. (2015).

0.14 wt% to 0.19 wt%, the same as the measured amount (Fig. 4).

	ΔNNO	SiO_2	TiO_2	Al_2O_3	FeO	MnO	MgO	CaO	Na_2O	K_2O	P_2O_5	S	Total*
lpm 1	1.34	46.19	3.75	15.68	9.93	0.20	6.39	10.14	4.07	2.00	1.17	0.22	93.75
		(0.25)	(0.10)	(0.14)	(0.36)	(0.08)	(0.10)	(0.25)	(0.05)	(0.20)	(0.06)	(0.02)	
lpm 2		47.93	3.10	17.22	10.06	0.31	3.72	8.46	4.81	2.34	1.82	0.11	96.23
		(0.98)	(0.15)	(0.39)	(0.19)	(0.07)	(0.15)	(0.62)	(0.62)	(0.700	(0.66)	(0.01)	
lpm 33		46.81	3.60	16.17	10.27	0.20	4.52	10.62	4.61	1.61	1.19	0.18	92.59
		(0.45)	(0.21)	(0.07)	(0.34)	(0.07)	(0.25)	(0.37)	(0.25)	(0.25)	(0.06)	(0.01)	
lpm 4		44.88	3.56	15.79	11.79	0.25	5.14	10.52	4.60	1.84	1.13	0.23	94.81
		(0.22)	(0.14)	(0.11)	(0.12)	(0.05)	(0.10)	(0.15)	(0.15)	(0.06)	(0.06)	(0.01)	
lpm 5		45.43	3.40	15.25	11.58	0.20	5.76	11.24	4.42	1.17	1.07	0.21	93.74
		(0.40)	(0.16)	(0.21)	(0.28)	(0.09)	(0.57)	(0.72)	(0.16)	(0.34)	(0.06)	(0.03)	
lpm 6		46.52	3.46	16.00	10.73	0.22	5.19	11.58	4.03	0.96	1.07	0.10	91.88
		(0.15)	(0.16)	(0.09)	(0.34)	(0.08)	(0.27)	(0.16)	(0.08)	(0.14)	(0.09)	(0.02)	
lpm 34		48.42	2.98	17.42	9.17	0.19	3.58	9.08	5.54	2.40	1.18	0.00	92.60
		(0.27)	(0.11)	(0.21)	(0.30)	(0.05)	(0.09)	(0.22)	(0.25)	(0.10)	(0.02)	(0.01)	
lpm 7	2.38	48.93	3.24	15.92	7.92	0.15	5.85	9.73	3.81	1.66	0.95	0.73	93.55
		(0.23)	(0.06)	(0.12)	(0.09)	(0.03)	(0.06)	(0.13)	(0.06)	(0.09)	(0.08)	0.04)	
lpm 8		46.13	3.52	15.36	7.95	0.21	6.24	10.93	4.44	1.94	1.05	0.86	93.00
		(0.28)	(0.14)	(0.10)	(0.26)	(0.02)	(0.17)	(0.23)	(0.09)	(0.17)	(0.09)	(0.06)	
lpm 9		48.78	2.97	17.36	6.71	0.20	4.61	8.66	5.50	2.38	1.38	0.57	94.81
		(0.15)	(0.10)	(0.21)	(0.21)	(0.07)	(0.18)	(0.22)	(0.07)	(0.14)	(0.13)	(0.03)	
lpm 13	3.30	50.68	2.45	16.17	6.10	0.20	6.42	9.62	3.75	1.72	0.99	0.75	92.63
		(0.35)	(0.11)	(0.22)	(0.30)	(0.08)	(0.09)	(0.14)	(0.42)	(0.06)	(0.05)	(0.04)	
lpm 14		49.60	2.47	17.28	5.29	0.24	5.53	10.32	4.65	1.48	1.20	0.75	91.99
		(0.21)	(0.16)	(0.22)	(0.19)	(0.09)	(0.32)	(0.42)	(0.12)	(0.13)	(0.12)	(0.04)	
lpm 15		48.12	2.87	16.15	5.89	0.19	6.44	10.76	4.68	1.93	1.19	0.69	92.01
		(0.33)	(0.16)	(0.10)	(0.20)	(0.07)	(0.26)	(0.14)	(0.07)	(0.18)	(0.06)	(0.05)	
lpm- 16		49.77	2.27	16.37	6.07	0.12	6.25	10.48	4.17	1.72	1.16	0.79	91.16
		(0.23)	(0.04)	(0.21)	(0.23)	(0.04)	(0.05)	(0.08)	(0.06)	(0.11)	(0.00)	(0.03)	
lpm 17		49.79	2.49	16.62	5.83	0.20	5.17	11.54	4.03	1.14	1.27	0.65	89.92
		(0.169	(0.12)	(0.37)	(0.23)	(0.11)	(0.58)	(0.75)	(0.33)	(0.29)	(0.09)	(0.09)	
lpm 18		51.87	2.29	18.26	5.17	0.26	4.07	9.96	4.39	1.58	1.46	0.33	89.41
		(0.31)	(0.30)	(1.05)	(0.52)	(0.07)	(0.90)	(0.46)	(0.45)	(0.23)	(0.10)	(0.03)	
lpm 19	4.10	52.79	1.73	17.04	5.24	0.17	5.83	9.19	3.97	1.80	0.85	0.68	91.44
		(0.15)	(0.08)	(0.23)	(0.09)	(0.07)	(0.06)	(0.52)	(0.03)	(0.24)	(0.04)	(0.05)	
lpm 20		51.66	1.89	17.67	4.74	0.22	5.52	10.07	4.32	1.37	1.21	0.64	90.53
		(0.09)	(0.07)	(0.10)	(0.07)	(0.04)	(0.34)	(0.42)	(0.05)	(0.12)	(0.10)	(0.01)	
lpm 21		55.88	1.42	19.71	3.35	0.23	1.33	7.77	5.52	2.01	1.51	0.58	91.59
		(0.19)	(0.13)	(0.58)	(0.44)	(0.05)	(0.11)	(0.38)	(0.10)	(0.17)	(0.14)	(0.05)	
lpm 22		51.50	1.69	17.57	5.13	0.25	3.71	12.64	4.20	0.65	1.22	0.71	90.99
		(0.19)	(0.08)	(0.39)	(0.19)	(0.07)	(0.53)	(0.63)	(0.11)	(0.08)	(0.04)	(0.04)	
lpmS 23		55.01	1.35	19.49	3.51	0.26	1.71	8.59	5.17	1.89	1.64	0.65	90.14
		(0.17)	(0.11)	(0.71)	(0.52)	(0.10)	(0.95)	(0.81)	(0.14)	(0.24)	(0.22)	(0.03)	
lpm S 24		56.03	1.52	20.19	3.74	0.20	1.68	6.69	4.98	2.76	1.38	0.38	89.50
		(0.45)	(0.13)	(1.25)	(0.47)	(0.09)	(0.64)	(0.70)	(0.29)	(0.13)	(0.13)	(0.03)	
lpmS 25		53.38	2.00	18.85	4.62	0.27	4.28	7.89	5.28	2.33	1.05	0.01	91.49
		(0.12)	(0.11)	(0.21)	(0.22)	(0.11)	(0.05)	(0.07)	(0.11)	(0.10)	(0.08)	(0.01)	
lpm 26	-0.48	46.28	3.88	16.78	8.89	0.22	5.88	10.28	4.45	1.77	1.24	0.12	92.87
		(0.12)	(0.06)	(0.22)	(0.11)	(0.09)	(0.06)	(0.06)	(0.05)	(0.10)	(0.12)	(0.01)	
lpm 27		47.16	3.50	17.35	10.19	0.24	4.53	9.66	4.00	1.99	1.18	0.10	94.19
		(0.38)	(0.20)	(0.52)	(0.36)	(0.14)	(0.37)	(0.49)	(0.77)	(0.06)	(0.07)	(0.01)	
lpm 28		45.26	3.86	15.22	11.65	0.21	5.77	11.31	3.72	1.57	1.13	0.13	93.35
		(0.07)	(0.15)	(0.32)	(0.26)	(0.05)	(0.07)	(0.17)	(0.19)	(0.06)	(0.10)	(0.01)	
lpm 29		44.24	3.77	15.16	12.64	0.21	5.75	11.40	3.89	1.55	0.94	0.19	92.82
		(0.10)	(0.06)	(0.06)	(0.18)	(0.04)	(0.23)	(0.27)	(0.09)	(0.25)	(0.06)	(0.03)	
lpm 30		44.59	3.93	15.02	12.36	0.20	5.34	11.83	3.89	1.42	0.95	0.19	93.35
		(0.14)	(0.12)	(0.23)	(0.26)	(0.05)	(0.14)	(0.23)	(0.09)	(0.11)	(0.08)	(0.03)	
lpm 32		46.09	4.34	15.85	9.92	0.14	5.38	13.09	3.29	0.79	1.01	0.01	92.35
		(0.64)	(0.15)	(0.14)	(0.75)	(0.05)	(0.81)	(1.24)	(0.17)	(0.18)	(0.06)	(0.01)	

223 *Table 3 Major elements compositions, normalized to 100% anhydrous, and S contents of quenched glasses; *Original total.*

224

4.2 Mass balance and ImageJ

For most experiments, the volumetric percentage of glass obtained by mass balance is similar to that calculated using ImageJ (Table 4). The mass balance estimates indicate that amphibole content peaks at 40 wt.%, while clinopyroxene abundance is generally below 10 wt% and not higher than 19 wt% (Table 4). Similarly, olivine proportion does not exceed 10 wt.%. The fact that amphibole proportion is higher than that in the rocks (<5 wt%, e.g. Ubide et al., 2023) reflects the lower temperature of our experiments.

The calculated wt.% of glass correlates well with P_2O_5 abundance, as P is incorporated only by apatite (SIb). The dashed line in SIb is calculated assuming perfectly incompatible behaviour of P_2O_5. Deviations from it signify apatite formation, which occurs after 20–30 wt.% crystallisation.

	Mass balance											ImageJ estimation
	Gl wt%	Ol wt%	Amph wt%	Cpx wt%	Fes wt%	Anhy wt%	Mt wt%	Ilm wt%	Ap wt%	Gl vol%	Sr	Gl %
lpm 1	75.6 (0.02)	<1 (0.01)	18.5 (0.03)	4.6 (0.01)	2.8 (0.002)	-	-	-	-	79.4	0.22	86.5
lpm 2	56.0 (0.01)	<1 (0.03)	33.4 (0.03)	8.2 (0.01)	1.1 (0.01)	-	1.7 (0.01)	-	-	61.0	0.18	55.1
lpm 33	75.1 (0.03)	3.6 (0.01)	15.9 (0.04)	3.0 (0.01)	-	-	2.4 (0.003)	-	-	79.1	0.41	72.2
lpm 4	78.6 (0.03)	3.6 (0.01)	10.0 (0.04)	4.4 (0.02)	1.3 (0.005)	-	1.9 (0.01)	-	-	82.6	0.02	84.3
lpm 5	86.6 (0.03)	2.5 (0.01)	7.8 (0.03)	0.2 (0.03)	-	-	2.9 (0.003)	-	-	89.5	0.53	72.2
lpm 6	77.7 (0.02)	4.8 (0.01)	15.8 (0.03)	<1 (0.01)	-	-	2.5 (0.003)	-	-	81.4	1.22	77.4
lpm 34	62.3 (0.02)	2.5 (0.004)	17.0 (0.03)	14.0 (0.01)	-	-	4.3 (0.003)	-	-	68.0	0.16	57.0
lpm 7	90.1 (0.01)	3.3 (0.002)	-	-	-	-	5.5 (0.003)	1.1 (0.002)	-	93.7	7.22	95.2
lpm 8	87.4 (0.01)	1.5 (0.003)	-	5.1 (0.009)	-	-	6.0 (0.002)	-	-	92.4	1.20	99.3
lpm 9	54.7 (0.03)	<1 (0.01)	26.1 (0.05)	11.8 (0.02)	-	-	8.5 (0.003)	-	-	77.9	0.08	68.2
lpm 13	89.9 (0.01)	1.8 (0.003)	-	-	-	-	12.2 (0.004)	<1 (0.003)	-	95.3	9.99	91.8
lpm 14	76.7 (0.01)	2.1 (0.003)	-	12.7 (0.01)	-	-	8.5 (0.002)	-	-	84.6	6.15	78.7
lpm 15	80.0 (0.01)	-	-	11.6 (0.01)	-	-	8.3 (0.002)	-	-	85.8	1.59	70.6
lpm 16	77.2 (0.01)	-	-	9.8 (0.01)	-	-	13.4 (0.003)	<1 (0.003)	-	84.5	0.80	84.5
lpm 17	79.9 (0.01)	2.1 (0.003)	-	4.3 (0.01)	-	-	7.0 (0.003)	-	-	86.8	1.54	84.6
lpm 18	51.5 (0.01)	-	37.1 (0.03)	1.6 (0.02)	-	-	9.8 (0.003)	-	-	60.8	3.10	72.3
lpm 19	89.5 (0.01)	7.4 (0.01)	-	<1 (0.02)	-	5.7 (0.004)	11.4 (0.003)	0.4 (0.003)	-	94.0	0.40	93.4
lpm 20	56.8 (0.02)	<1 (0.01)	33.3 (0.04)	3.6 (0.01)	-	-	12.1 (0.004)	<1 (0.003)	-	63.4	1.07	68.5
lpm 21	43.0 (0.01)	-	39.7 (0.02)	9.0 (0.01)	-	-	8.4 (0.002)	-	-	48.57	0.96	59.8
lpm 22	77.8 (0.01)	6.1 (0.003)	-	2.5 (0.01)	-	-	13.6 (0.002)	-	-	86.6	4.48	84.7
lpm 23	47.6 (0.01)	-	27.9 (0.01)	13.8 (0.01)	-	-	10.7 (0.002)	-		57.5	2.51	62.8
lpm 24	45.1 (0.01)	-	31.1 (0.03)	12.0 (0.04)	-	-	10.3 (0.002)	-	1.6 (0.004)	51.7	0.97	55.6
lpm 25	57.3 (0.01)	-	14.4 (0.01)	18.8 (0.01)	-	-	9.5 (0.002)	-	-	67.2	1.27	66.4
lpm 26	77.1 (0.0)	0.8 (0.01)	8.4 (0.04)	9.6 (0.01)	4.1 (0.002)	-	-	-	-	81.5	0.26	72.3
lpm 27	67.0 (0.02)	3.2 (0.004)	18.8* (0.04)	<1 (0.02)	2.1 (0.002)	-	-	-	-	71.7	1.22	82.5
lpm 28	99.0 (0.13)	<1 (0.01)	<1 (0.14)	-	-	-	<1 (0.003)	-	-	99.0	1.19	94.8
lpm 29	93.1 (0.01)	4.8 (0.003)	-	<1 (0.01)	1 (0.003)	-	-	-	-	95.0	0.20	89.5
lpm 30	96.6 (0.03)	6.6 (0.003)	-	<1 (0.01)	0.2 (0.003)	-	0.5 (0.01)	-	-	97.5	0.53	86.5
lpm 32	80.0 (0.12)	9.3 (0.005)	17.5* (0.13)	<1 (0.01)	-	-	1.7 (0.01)	-	-	83.1	2.96	97.8

Table 4. Phase proportions calculated by mass balance and image analyses (glass, using ImageJ software).

**Amphibole partly of inferred quench origin.*

5. Discussion

Our experiments emphasise the control of fO_2 on the S-carrying capacity of silicate melts, as shown in many previous studies (e.g.,Carroll and Rutherford, 1985; Luhr, 1990; Scaillet et al., 1998; Jugo et al., 2005). The effects of sulphur on phase relations are subtle and complex, depending on the fO_2 of the experiments. In particular, amphibole is unstable at intermediate fO_2, between NNO+2.38 and NNO+4.10, and S-rich conditions, while sulphide precipitates only below NNO+1.5. The minor differences noted between the S- and FeS-doped series may be explained by the presence of higher iron abundance in the latter case. Sulphur does not appear to affect significantly the composition of individual phases, except for a tendency of FeMg silicate phases to become more Mg-rich with S addition. In contrast, oxygen fugacity does affect phase compositions, in particular olivine and glass, whose Mg# increases markedly under more oxidising conditions in both the S-doped and FeS-doped experiments.

The mass balance data also show no systematic effect of sulphur on phase proportions in the different experiments, aside from the obvious cases of sulphide or anhydrite. Here again, oxygen fugacity appears to exert the stronger influence. As expected, the amounts of oxides, both titanomagnetite and ilmenite, increase from reducing to oxidising conditions (Table 4). In detail,

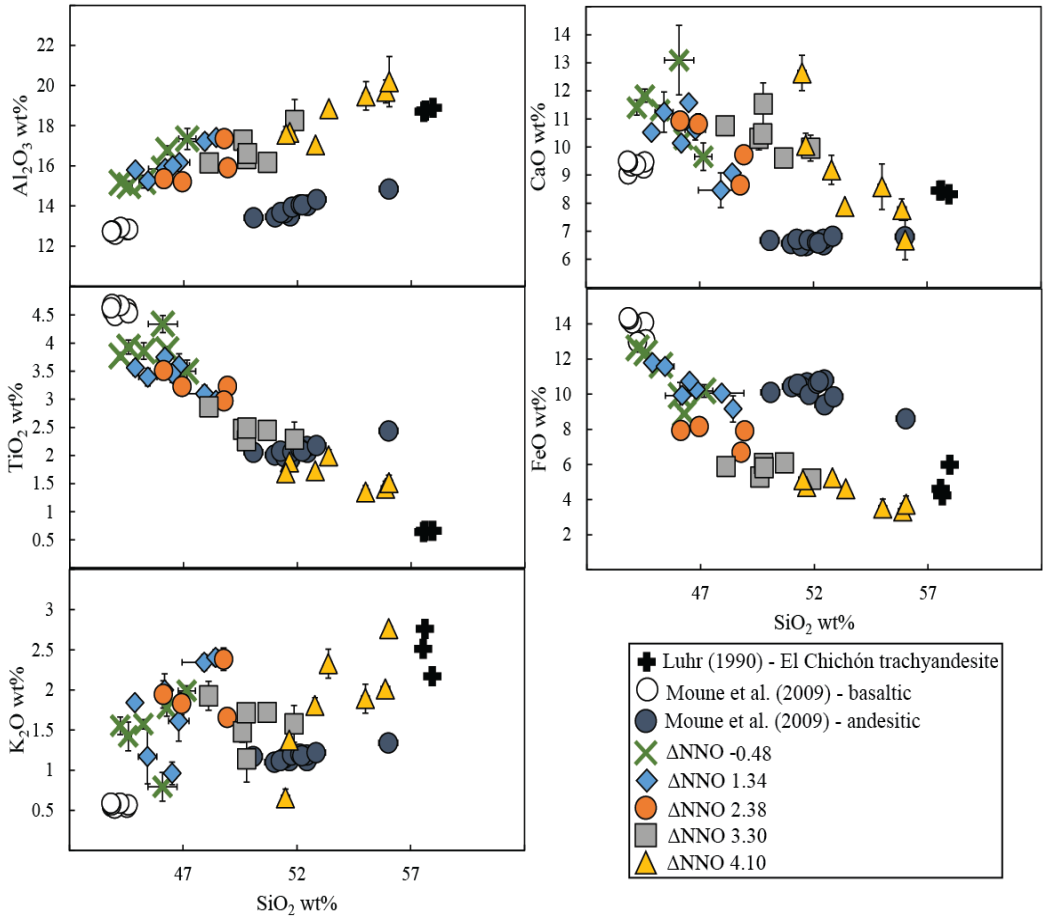

Fig. 5 Concentration of major element versus SiO_2 wt.%. The experiments are compared to the water-saturated, 1050°C and 200-300 MPa experiments of Moune et al. (2009) and the composition A (trachyandesite) performed at 1000°C, 200 MPa from Luhr (1990).

amphibole abundance increases slightly in more oxidised runs than in reduced ones, but with no clear difference between sulphur-rich and sulphur-poor charges. This confirms that oxygen fugacity, not the amount of sulphur in the system, exerts the stronger control on phase proportions.

From the perspective of sulfur content in the residual glass, both sets of experiments show a consistent pattern of increasing sulfur content with elevated fO_2. The changes in melt composition resulting from fO_2 variation are perhaps best illustrated by changes in Ti and Fe contents: from NNO-0.48 to NNO+4.10, both the TiO_2 and FeO abundances in the glass decrease by 75 wt%, reflecting substantial crystallisation of Fe-Ti oxides. This increase in crystallisation is accompanied by an increase in abundances of Al_2O_3 and SiO_2 in the glass, owing to the lack of plagioclase crystallisation. These significant changes in melt composition do not, however, seem to affect the overall positive effect that fO_2 has on S concentrations.

Our results can be compared with sulphur solubility experiments performed at comparable P-T-H_2O conditions on hydrous basaltic-andesitic magmas erupted in contrasting geodynamic contexts: i) at Hekla volcano in 2000, which is taken to here represent mid-ocean ridge volcanism, though interaction with plume material is possible (Moune et al., 2009); ii) the trachyandesite magma erupted at El Chichón volcano in 1982, which belongs to an arc setting (Luhr, 1990) though some rift related processes are likely (Arce et al., 2014). The water-saturated, 1050°C and 200–300 MPa experiments of Moune et al., (2009), and the composition A (trachyandesite) performed at 1000°C, 200 MPa from Luhr (1990), are compared with our data in Fig. 5. At any given SiO_2, differences in some oxide contents (e.g., CaO, Al_2O_3) are evident. These can be attributed to bulk compositional effects (Fig. 5) and to slightly different experimental conditions which impart different degrees of crystallization. The broad correspondences remain when oxygen fugacity is considered (Figure SIc). The TiO_2 content of the andesitic charges of Moune et al (2009) and Luhr (1990) are lower than ours, reflecting the lower Ti content of the corresponding starting materials. This is particularly evident in the Luhr (1990) experiments, in which the concentration of TiO_2 in the starting composition is so low that no difference exists between reduced and oxidised conditions. Based on these data, it appears that the presence of sulphur does not significantly affect the concentrations of the major elements of residual melts. Irrespective of geodynamic context, the factor that most influences melt composition is oxygen fugacity.

As in many previous studies(e.g., Carroll and Rutherford, 1985; Liu et al., 2007; Moune et al., 2009), our experiments reveal a significant difference in the amount of sulphur in the glasses between low and high fO_2 experiments (Fig. 6). At low fO_2, the sulphur concentrations in the glasses measured by Moune et al (2009) and Luhr (1990) are comparable to those found in our experiments, most falling in the interval 1000–2500 ppm. Furthermore, as noted by Moune et al. (2009), at fO_2 between NNO-0.48 and NNO1.34, sulphur abundance in the glass increases in proportion to the increase of added sulphur, until bulk S exceeds 0.5 wt.% (Fig 6). Thereafter, the S content in the glass levels off at 2000±100 ppm. At fO_2 above NNO+2.38, a similar pattern is observed with a positive trend up to about 1 wt.% sulphur added, at which point the dissolved S levels off at 0.7 wt%.

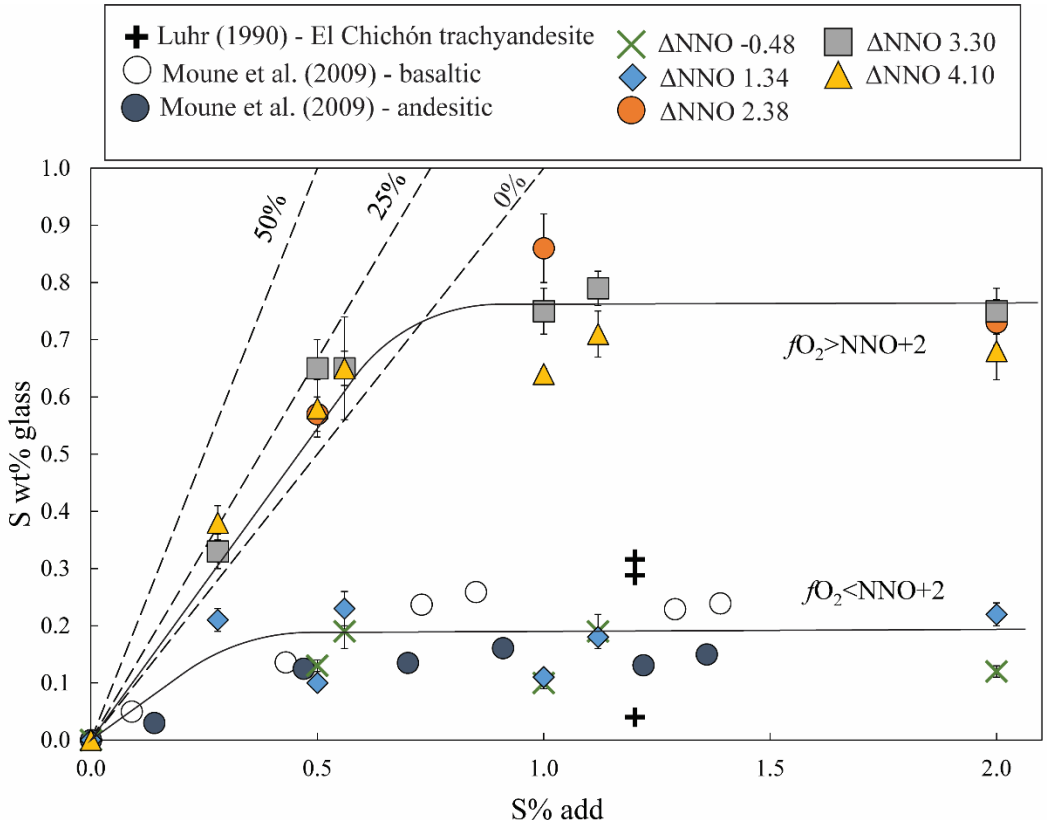

Fig.6 Sulphur concentration in the melt versus the amount of sulphur added in the runs. The experiments are compared to the water-saturated, 1050°C and 200-300 MPa experiments of Moune et al. (2009) and the composition A (trachyandesite) performed at 1000°C, 200 MPa from Luhr (1990). The dashed trendlines are calculated assuming an incompatible behaviour of S at 50%, 25% and 0% of crystallization.

The experiments of Luhr (1990) carried out under oxidised conditions resulted in lower S concentrations in the glass than we obtained for the same amount of sulphur added. Anhydrite crystallization in the Luhr (1990) runs, which did not occur in our experiments under the same conditions, likely explains this. The levelling off of both trends at high bulk S contents likely results from the buffering effect of other S-bearing phases. In addition to fluid, under reducing conditions this would be sulphide, while under oxidising contions this would be anhydrite. Oxidised charges with less than 0.5 wt.% added S fall on, or close to, the 1-to-1 correlation line, which shows that under these conditions a significant proportion of S resides in the melt phase (those data that fall above the 1/1 line reflect the amount of crystallisation of charges).

5.1 Significance for understanding the La Palma 2021 eruption

The pre-eruptive fO_2 of Cumbre Vieja 2021 basanite has been broadly constrained from V systematics in olivine to fall between NNO+0.6 and NNO+1.3 (Day et al., 2022). We note however that a recent reassessment of V behaviour has concluded that current formulations of this oxybarometer tend to overestimate fO_2 by up to 0.7 log unit in hydrous basalts (Erdmann et al., 2024), which would bring the La Palma magma redox state into the NNO-NNO+1 range.

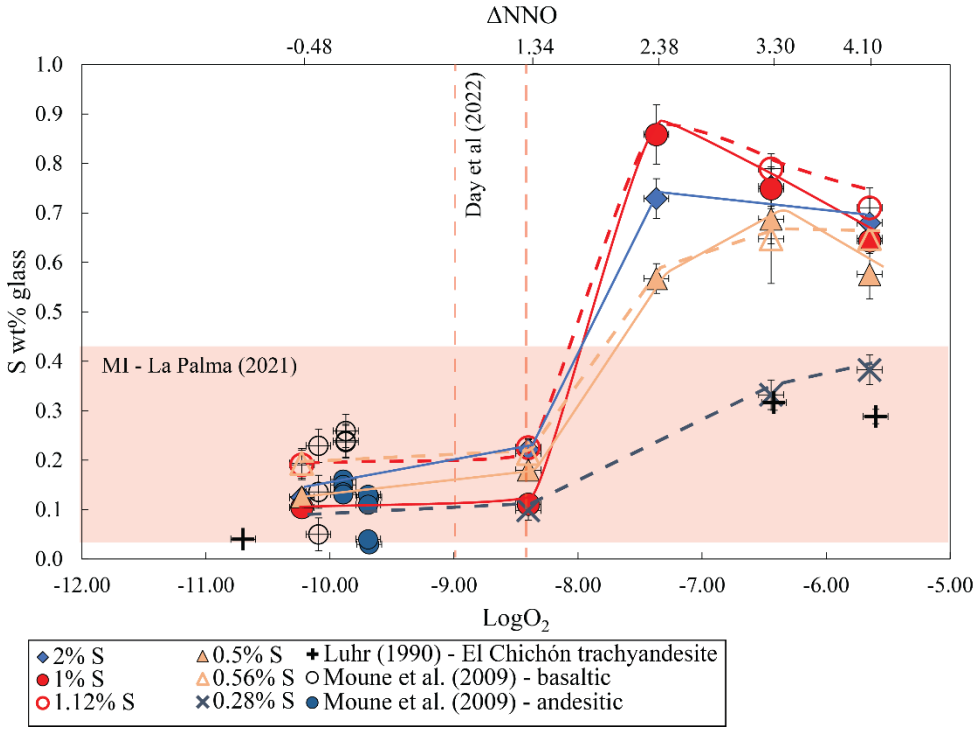

Fig. 7 Sulphur concentration in the melt versus logfO_2. The experiments are compared to the water-saturated, 1050°C and 200-300 MPa experiments of Moune et al., 2009 and the composition A (Trachyandesite) performed at 1000°C, 200 MPa from Luhr, 1990; MI-La Palma (2021) = S wt% in melt inclusions (Castro and Feisel, 2022; Burton et al., 2023; Dayton et al., 2024).

Considering a NNO-NNO+1.3 range, our data indicate that under these conditions the bulk magma S content was ~2500–5000 ppm, a significant part of which was dissolved in the melt, broadly consistent with melt inclusion analyses (Fig.7) (e.g., Castro and Feisel, 2022; Burton et al., 2023; Dayton et al., 2024). Note that the highest S content so far measured in melt inclusions (4800 ppm, Burton et al., 2023) points to fO_2 at the upper end of the range inferred from V in olivine (Fig. 10), or higher temperatures. The occasional occurrence of sulphides (as inclusions in phenocrysts) in erupted products (Andujar et al., submitted) is consistent with our experiments at NNO+1.34, although the absence of sulphide in the matrix glass suggests that the erupting magma was not saturated in sulphide.

Our experiments show that to achieve the observed S content analysed in melt inclusions of La Palma 2021 basanite (around 3000 ppm S) at the inferred pre-eruptive fO_2 between NNO+0.6 and NNO+1.6 (Day et al., 2022), the fS_2 should be around 0.1–1 MPa, as recorded by the composition of pyrrhotite in our run products (Table 2).

Using these constraints, in what follows we have have carried out calculations aimed at modelling the fluid phase composition for three different scenarios: (1) we have first calculated the fluid composition at equilibrium with the basanite magma lying in the crustal reservoir, which is inferred to lie at ~ 300 MPa, based on seismic source locations and petrological arguments (e.g., D'Auria et al., 2022; Del Fresno et al., 2023b; Ubide et al., 2023; Dayton et al., 2024; Andujar et al., submitted). (2) We next perform calculations of magma degassing during uprise, starting at 300 MPa with variable amount of exsolved fluid. (3) Finally, we simulate degassing from higher pressures (i.e. deeper levels) and higher temperature (about 1125°C), in keeping with the elevated CO_2 dissolved contents (up to 1.2 wt%) retrieved from olivine inclusions (e.g., Zanon et al., 2023; Dayton et al., 2024) and seismic data (e.g., D'Auria et al., 2022; Del Fresno et al., 2023) which point to a mantle source at 400-800 MPa.

(1) For the first step, we use the following constraints: a pre-eruptive dissolved CO_2 content ranging from 3000–5000 ppm, and a dissolved H_2O_{melt} of 1–3 wt%, drawing on melt inclusion analyses (e.g., Burton et al., 2023; Dayton et al., 2023). We perform calculations at 1080°C, which corresponds to the inferred temperature for the basaltic magma at equilibrium with amphibole ((González-García et al., 2023)González-García et al., 2023; Sandoval-Velasquez et al., 2023; Andujar et al., submitted), using an MRK equation of state for fluid coupled to the S solubility model of Lesne et al. (2015), calibrated for alkali-rich

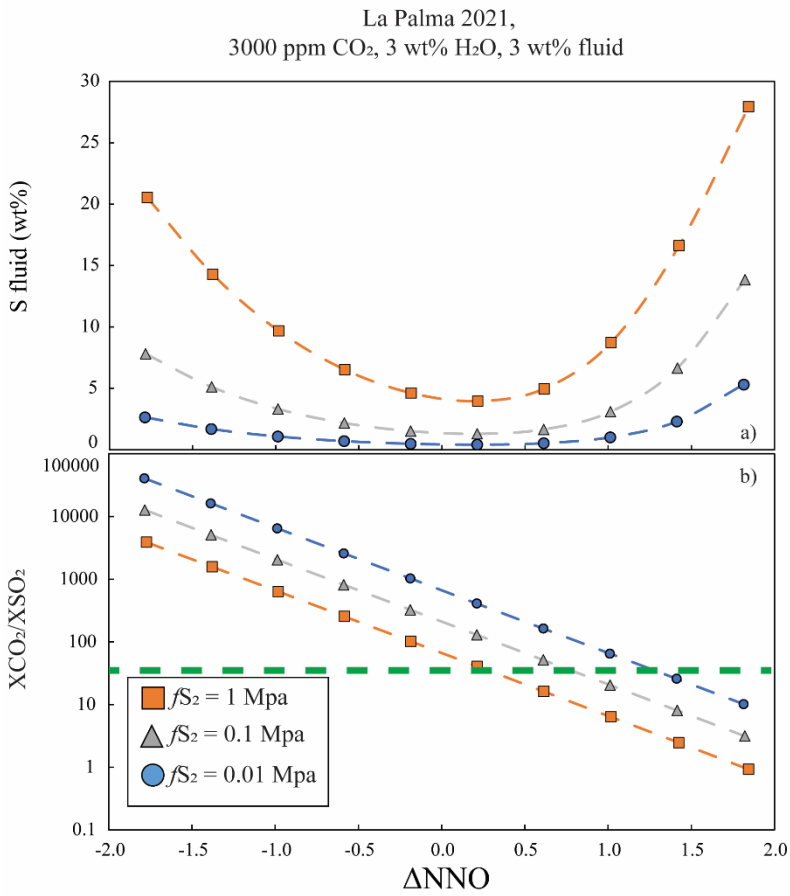

Fig. 8 (a) Evolution of the S content of the excess fluid in the reservoir at 300 MPa with fO_2. (b) Evolution of the ratio XCO_2/XSO_2 of the fluid with ΔNNO. The calculations have been made at three different fS_2; The thick green line shows the XCO_2/XSO_2 ratio of volcanic gases measured at la Palma during explosive emissions (Burton et al., 2023). See text for details.

basalt melts, and to the CO_2-H_2O solubility model of Jímenez-Mejías et al. (2021), calibrated for a basanite from the Canary islands. The calculation then yields the saturation pressure in H_2O, CO_2, SO_2 and H_2S fluid species.The key assumption is that of equilibrium between the fugacities of volatiles in the fluid with those in the melt (e.g., Lesne et al., 2015). Given uncertainty in the magma redox state, and in its possible variation during decompression (e.g., Burgisser and Scaillet, 2007; Moussallam et al., 2016), we performed the calculations for a range of fO_2 between NNO-2 and NNO+2. Fig 8a shows the variation of S content of the fluid in the reservoir at 300 MPa with fO_2, calculated for three different fS_2. This calculation gives the composition of fluids at the surface if they could leave the crustal reservoir on their own, i.e. without being accompagnied by melts, and traversing the crustal section unmodified. Although this scenario is possibly not directly applicable to the La Palma 2021 eruption, it provides context for the interpretation of gas monitoring during repose periods. In the range of fO_2 inferred by Day et al. (2022), the S content of the fluid falls between 1 and 10 wt%, depending on fS_2, comparable with S contents calculated for more silicic compositions (e.g., Scaillet et al., 2003) and to that calculated by mass balance

for most of our experiments (Table 2). The calculations further show that XCO_2/XSO_2 progressively decreases as fO_2 increases (Fig. 8b). In the fO_2 interval NNO+0.7 to NNO+1.3, XCO_2/XSO_2 ranges from ~ 2 up to ~ 100, within the range of measurements of volcanic gas emissions during the 2021 La Palma eruption (Burton et al., 2023). Measured ratios range from to 35 for explosive activity down to less than 10 for effusive emissions (Burton et al., 2023), and the higher end is to be favoured as a characteristic of gas-rich magma, presumably of deeper provenance.

(2) We next consider degassing during magma ascent, especially of S and H_2O, which can exsolve and separate from the melt extensively near the surface (Oppenheimer et al., 2014). The full calculation should also take into account the possible role of an excess fluid in the crustal reservoir. For instance, the bulk CO_2 content of La Palma magma has been estimated to be at 4±1.5 wt% based on the measured S emissions and the average XCO_2/XSO_2 ratio (Burton et al., 2023). Taking a conservative value of 3 wt% fluid (with 3 wt% H_2O and

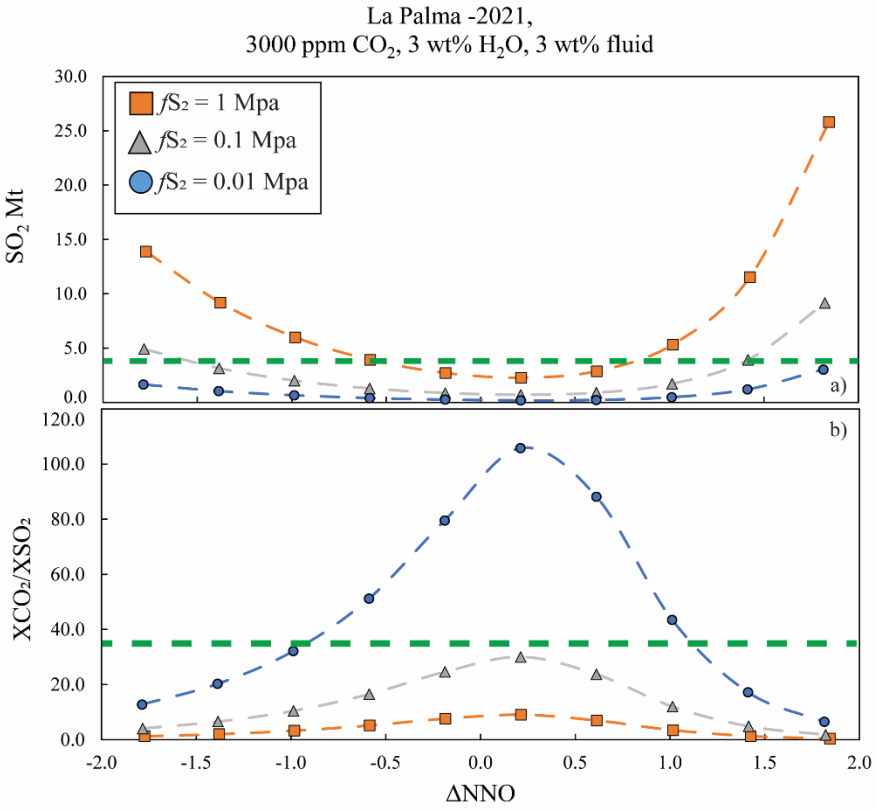

Fig. 9 (a) Evolution of total amount of SO_2 degassed by 0.2 km^3 of basanite magma with fO_2 expressed as ΔNNO. (b) Evolution of the XCO_2/XSO_2 ratio of the gas emitted at the vent with ΔNNO. The calculations have been performed at 1080°C.

3000 ppm CO_2 dissolved in melt, which correspond to the volatile contents of a fluid saturated basanite at 300 MPa), we calculate as a function of oxygen fugacity both the total

amount of S released by the 0.2 km^3 of erupted magma, and the XCO_2/XSO_2 ratio of the gas at the vent (i.e. melt+fluid), accounting for the 400– 600 ppm of S that remains in matrix glass (Fig. 12). With these constraints and assuming an fO_2 of ~ NNO+1, 2-4 Mt SO_2, we find that the pre-eruptive magma must have had an fS_2 in the range 0.1-1 MPa (Fig. 9a). A fS_2 significantly lower than 0.1 MPa will fall short in reproducing this figure. With respect to the final XCO_2/XSO_2 ratio (i.e. the one measured at the vent), the same set of calculations shows that such a ratio displays a bell-shaped pattern, with a maximum in between NNO and NNO+0.5 (fig.9b). For fS_2 values in the range 0.1-1 MPa, the maximum possible XCO_2/XSO_2 ratio is about 30, lying slightly above NNO, i.e. at an fO_2 more reduced than that retrieved from V systematic.

It is also interesting to consider the XH_2O/XSO_2 ratio, which was also measured during La Palma 2021 eruption (Burton et al., 2023). The variation of this ratio with fO_2 (as for XCO_2/XSO_2) with the amount of excess fluid in the reservoir is shown in Fig. 10b. Here the calculations are made for a magma at 300 MPa with 4000 ppm CO_2, 2 wt% H_2O and for fS_2=0.2 MPa, at 1080°C, also consistent with available melt inclusion and phase equilibrium constraints for the top portion of the plumbing system (González-García et al., 2023; Sandoval-Velasquez et al., 2023; Andujar et al., submitted). As with the previous calculations, both ratios exhibit a similar bell shaped trend with fO_2. They are both sensitive to the amount of free fluid: as it increases, so the XH_2O/XSO_2 ratio drops, while the XCO_2/XSO_2 increases, due to the contrasting H_2O and CO_2 contents in melt and fluid phases. Gas emissions during the most explosive phase of La Palma eruption had an

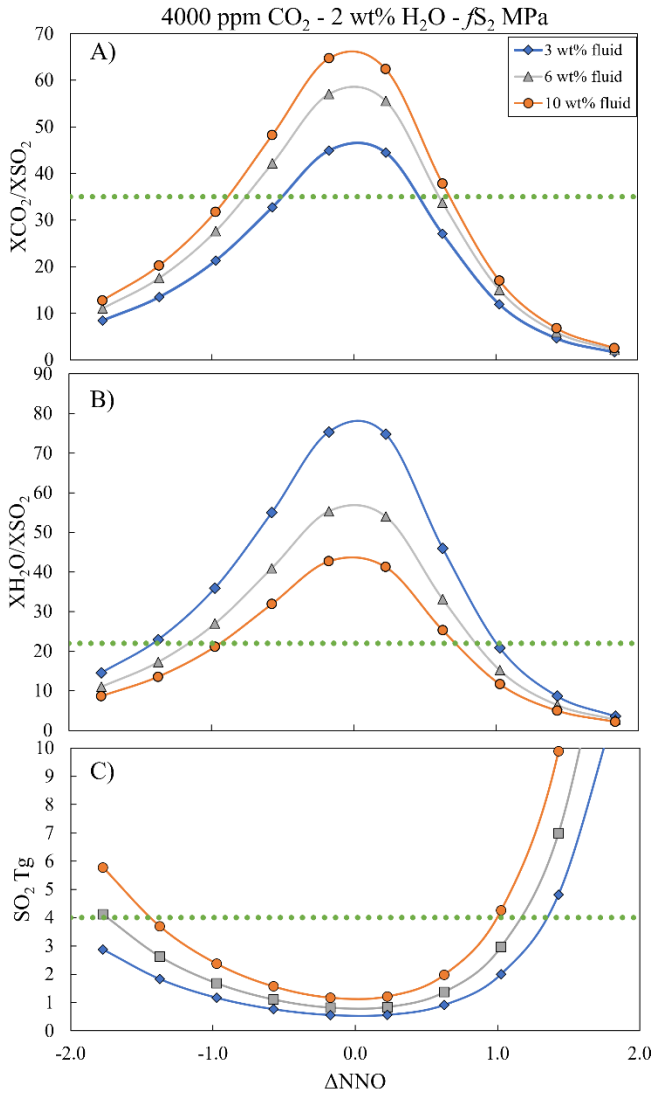

Fig. 10. Evolution of the XH_2O/XSO_2 (a) and XCO_2/XSO_2 (b) ratios of gases vented at 0.1 MPa with fO_2, for different amounts of exsolved fluid in the reservoir at 300 MPa. (c) Evolution of the mass of SO_2 produced for the three different amounts of fluid. In all panels the thick horizontal green dashed line indicates the measured value of the corresponding parameter.

XCO_2/XSO_2 of ~ 35 and an XH_2O/XSO_2 ratio of ~ 22 (Burton et al., 2023). For the conditions shown in Fig. 10, these ratios are reproduced at around NNO+0.5 to NNO+1 for 6 wt% excess fluid, broadly consistent with previous inferences. Clearly, the amount of SO_2 released increases with the amount of pre-eruptive fluid in the crustal reservoir (Fig. 13c). For this set of conditions, fO_2 in the range NNO+1 to NNO+1.5 are required to yield 4 Tg SO_2. These calculations point therefore to the presence of a significant amount of free fluid in the plumbing system, as indicated by previous work (e.g., Burton et al., 2023; Sandoval-Velasquez et al., 2023; Zanon et al., 2024)).

(3) The last set of calculations explores the deeper part of the plumbing system. As noted earlier, melt inclusions hosted by olivine record a range of dissolved CO_2, up to 5000 ppm (e.g., Dayton et al., 2024). If account is made for the occurrence of exsolved fluid in the

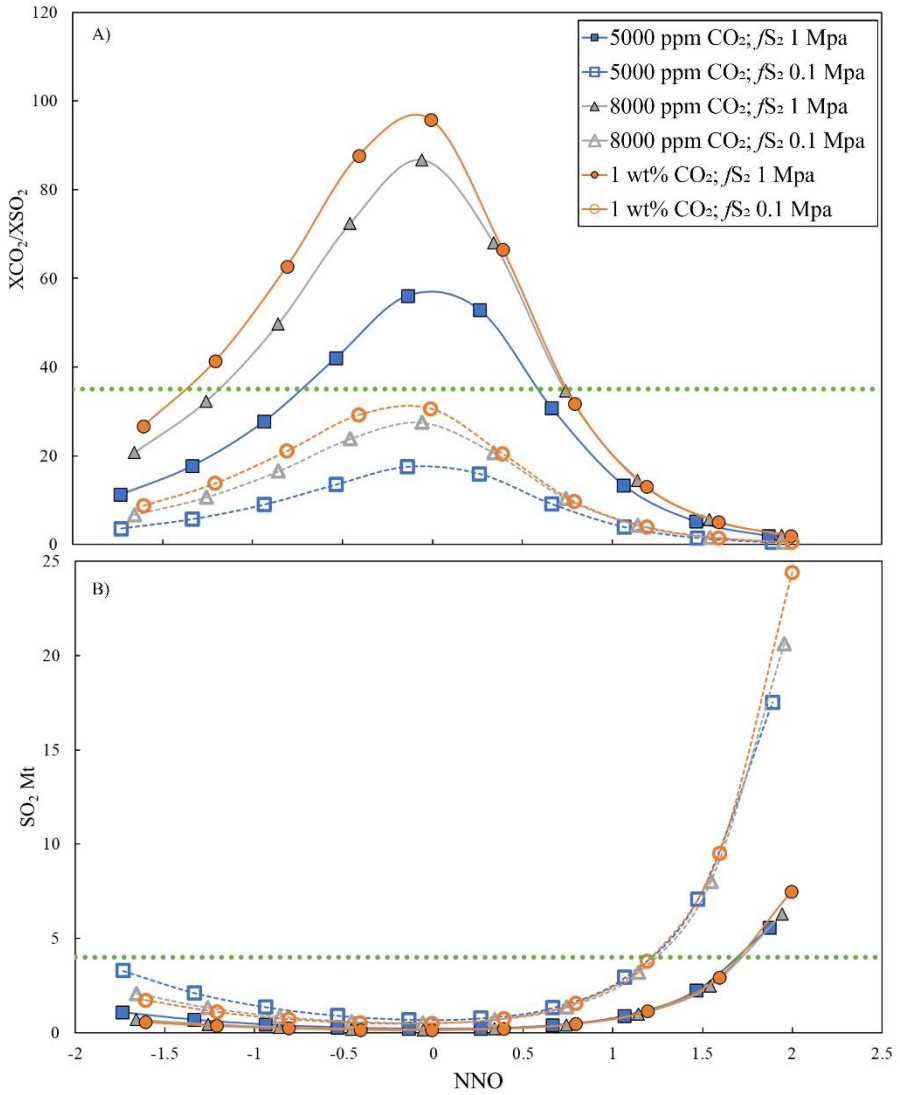

Fig. 11(a) Evolution of total amount of SO_2 degassed by 0.2 km^3 of basanite magma with fO_2 expressed as ΔNNO with increasing CO2 from 5000 ppm to 10000ppm. (b) Evolution of the XCO_2/XSO_2 ratio of the gas emitted at the vent with ΔNNO with increasing CO2 from 5000 ppm to 10000ppm.The calculations have been performed at 1125°C. In all panels the measured values of the corresponding parameter are in green dashed line (burton et al.,2023).

melt inclusions, the CO_2 content rises up to 1.2 wt% (Dayton et al., 2024), underscoring the deep mantle provenance of some of the magma erupted during the eruption. We have therefore also carried out calculations using higher dissolved CO_2, from 5000 to 10000 ppm (corresponding to pressures in the range 400-800 MPa). We keep the excess fluid at 3 wt% as in most calculations above and the amount of H_2O dissolved at 3 wt% (hence the total amount of volatiles sums up to over 6 wt%). Results are shown on figure 11. In terms of XCO_2/XSO_2, increasing pressure makes high fS_2 (1 MPa) less likely than a moderate one (0.1 MPa), since the familly of curves corresponding to fS_2=1MPa does not allow to reproduce the observed XCO_2/XSO_2 ratio of vented gases. Note that for an fS_2=0.1 MPa, the intersection happens at around NNO+1, which is an fO_2 slightly lower than the one inferred by Day et al. (2022).

For what regards the amount of SO_2 released, a magma with an fS_2 of 1 MPa would require an fO_2 slightly over NNO, while that with an fS_2 of 0.1 MPa would require slightly more oxidizing conditions, both fS_2 being compatible with the inferred range of redox state of La Palma magma (Day et al., 2022).

The above sets of calculations show that reproducing the observations reported for La Palma eruption, in particular the S content of melt inclusions, the gas composition, and the amount of S released, requires a subtle combination of fO_2, fS_2 and amount of fluid of the magma (in addition to T and P). Elevated S contents in the melt point to fO_2 conditions above NNO (Fig.6). The fS_2 should be in the vicinity of 0.1 MPa in order to reproduce the amount of SO_2 released (Fig 8a, 10c). An fS_2 too high will not be compatible with the observed XCO_2/XSO_2 ratio, in particular if the majority of outgassed sulphur is sourced from magma of deep mantle provenance (Fig 11). The amount of fluid in the reservoir is also critical if the final fluid released is to have an XH_2O/XSO_2 lower than XCO_2/XSO_2, as observed. According to our calculations, amounts of fluid significantly below 5 wt% (at 300 MPa) cannot satisfy this constraint (Fig. 10). An XH_2O/XSO_2 ratio of 22 and an XCO_2/XSO_2 ratio of 35 requires fO_2 to be ~ NNO+0.6, which is lower than inferred, and which would not sustain elevated S content in the melt (Fig. 6). This illustrates the challenge of delineating conditions that satisfy all observations. Beyond model uncertainties, such discrepancies may also reflect fractionation of gases during magma ascent, either near the surface (Burton et al., 2023), or deeper in the plumbing system. Uncertainties in magma's fO_2 remain large also and more work is needed to refine La Palma redox state, given the importance of this parameter on S behaviour. An additional caveat is that observed gases at La Palma likely represent the mixture of volatiles sourced from magma already stagnating in the reservoir, possibly years before the eruption (e.g., Day et al., 2022; Andujar et al., submitted), as well as mantle-derived volatile-rich magmas (Zanon et al., 2024; Dayton et al., 2024), injected shortly before or during eruption. Such processes, likely in play, are not captured by our treatment.

6. Conclusions

We have shown that the composition of the residual glass as well as the phase relationships and their proportions are primarily influenced by oxygen fugacity, but also by the amount of sulphur in the system, though to a lesser extent. Similarly, our experiments emphasise the considerable influence of fO_2 on the solubility of S in silicate melts (Figs. 5,6). Between NNO-0.48 and NNO1.34, the maximum S concentration in the residual glass is 0.2±0.01 wt%, while at oxygen fugacity above NNO+2.38, the maximum value is 0.7–0.8 wt%. These limits are imposed by the buffering effect of sulphide/sulphate phases in addition to the fluid.

Modelling of the fluid phase composition using an MRK equation of state for fluid and the models of Lesne et al. (2015) and Jiménez-Mejías et al. (2021) for volatile solubilities, shows that the S content of the fluid lies between 1 and 10 wt%, depending on fS_2. Overall, the calculations show that in order to expel 2-4 Mt of SO_2, the pre-eruptive magma must have had a fS_2 at the 0.1 MPa level (Fig. 11a) with an fO_2 above NNO, in general agreement with the oxidised character inferred for hot spot basalts (Moussallam et al., 2019), and coexisted with a significant amount of exsolved fluid in the crustal reservoir.

Acknowledgement

Acknowledge support from both LabEx VOLTAIRE (ANR-10-LABX-100-01) and EquipEx PLANEX (ANR-11-EQPX-0036) projects. We thank Mike Burton and an anonymous reviewer for their constructive comments which helped to improve significantly the manuscript, as well as the editorial handling of Sonia Calvari.

465

References

Albarède, F., 1996. Introduction to geochemical modeling, 1. paperback ed. (with corr.). ed. Cambridge Univ. Press, Cambridge.

Albertos, V.T., Hernández, P.A., Melián, G.V., Álvarez Díaz, A.J., Martín-Lorenzo, A., Padrón, E., Pérez, N.M., 2023. Diffuse CO2 and H2S degassing from Tajogaite volcanic cone, La Palma, Canary Islands (other). oral. https://doi.org/10.5194/egusphere-egu23-9916

Andújar, et al., 2024. Evolution of the crustal reservoir feeding La Palma 2021 eruption. Insights from phase equilibrium experiments and petrologically derived time scales. J. Volcanol. Geotherm. Res. submitted

Arce, J.L., Walker, J., Keppie, J.D., 2014. Petrology of two contrasting Mexican volcanoes, the Chiapanecan (El Chichón) and Central American (Tacaná) volcanic belts: the result of rift- *versus* subduction-related volcanism. Int. Geol. Rev. 56, 501–524. https://doi.org/10.1080/00206814.2013.879375

Bonadonna, C., Pistolesi, M., Biass, S., Voloschina, M., Romero, J., Coppola, D., Folch, A., D'Auria, L., Martin-Lorenzo, A., Dominguez, L., Pastore, C., Reyes Hardy, M., Rodríguez, F., 2022. Physical Characterization of Long-Lasting Hybrid Eruptions: The 2021 Tajogaite Eruption of Cumbre Vieja (La Palma, Canary Islands). J. Geophys. Res. Solid Earth 127, e2022JB025302. https://doi.org/10.1029/2022JB025302

Boulliung, J., Wood, B.J., 2023. Sulfur oxidation state and solubility in silicate melts. Contrib. Mineral. Petrol. 178, 56. https://doi.org/10.1007/s00410-023-02033-9

Burgisser, A., Scaillet, B., 2007. Redox evolution of a degassing magma rising to the surface. Nature 445, 194–197. https://doi.org/10.1038/nature05509

Burton, M., Aiuppa, A., Allard, P., Asensio-Ramos, M., Cofrades, A.P., La Spina, A., Nicholson, E.J., Zanon, V., Barrancos, J., Bitetto, M., Hartley, M., Romero, J.E., Waters, E., Stewart, A., Hernández, P.A., Lages, J.P., Padrón, E., Wood, K., Esse, B., Hayer, C., Cyrzan, K., Rose-Koga, E.F., Schiavi, F., D'Auria, L., Pérez, N.M., 2023. Exceptional eruptive CO2 emissions from intra-plate alkaline magmatism in the Canary volcanic archipelago. Commun. Earth Environ. 4, 467. https://doi.org/10.1038/s43247-023-01103-x

Carracedo, J.C., Badiola, E.R., Guillou, H., de La Nuez, J., Perez Torrado, F.J., 2001. Geology and volcanology of la Palma and El Hierro, Western Canaries. Estud. Geol.-Madr. 57, 175–273.

Carroll, M.R., Rutherford, M.J., 1988. Sulfur speciation in hydrous experimental glasses of varying oxidation state; results from measured wavelength shifts of sulfur X-rays. Am. Mineral. 73, 845–849.

Carroll, M.R., Rutherford, M.J., 1985. Sulfide and sulfate saturation in hydrous silicate melts. J. Geophys. Res. Solid Earth 90. https://doi.org/10.1029/JB090iS02p0C601

Castro, J.M., Feisel, Y., 2022. Author Correction: Eruption of ultralow-viscosity basanite magma at Cumbre Vieja, La Palma, Canary Islands. Nat. Commun. 13, 3929. https://doi.org/10.1038/s41467-022-31649-x

Clemente, B., Scaillet, B., Pichevant, M., 2004. The Solubility of Sulphur in Hydrous Rhyolitic Melts. J. Petrol. 45, 2171–2196. https://doi.org/10.1093/petrology/egh052

D'Auria, L., Koulakov, I., Prudencio, J., Cabrera-Pérez, I., Ibáñez, J.M., Barrancos, J., García-Hernández, R., Martínez Van Dorth, D., Padilla, G.D., Przeor, M., Ortega, V., Hernández, P., Peréz, N.M., 2022. Rapid magma ascent beneath La Palma revealed by seismic tomography. Sci. Rep. 12, 17654. https://doi.org/10.1038/s41598-022-21818-9

Day, J.M.D., Troll, V.R., Aulinas, M., Deegan, F.M., Geiger, H., Carracedo, J.C., Pinto, G.G., Perez-Torrado, F.J., 2022. Mantle source characteristics and magmatic processes during the 2021 La Palma eruption. Earth Planet. Sci. Lett. 597, 117793. https://doi.org/10.1016/j.epsl.2022.117793

Dayton, K., Gazel, E., Wieser, P., Troll, V.R., Carracedo, J.C., La Madrid, H., Roman, D.C., Ward, J., Aulinas, M., Geiger, H., Deegan, F.M., Gisbert, G., Perez-Torrado, F.J., 2023. Deep magma

storage during the 2021 La Palma eruption. Sci. Adv. 9, eade7641. https://doi.org/10.1126/sciadv.ade7641

Dayton, K., Gazel, E., Wieser, P.E., Troll, V.R., Carracedo, J.C., Aulinas, M., Perez-Torrado, F.J., 2024. Magmatic Storage and Volatile Fluxes of the 2021 La Palma Eruption. Geochem. Geophys. Geosystems 25, e2024GC011491. https://doi.org/10.1029/2024GC011491

Del Fresno, C., Cesca, S., Klügel, A., Domínguez Cerdeña, I., Díaz-Suárez, E.A., Dahm, T., García-Cañada, L., Meletlidis, S., Milkereit, C., Valenzuela-Malebrán, C., López-Díaz, R., López, C., 2023a. Magmatic plumbing and dynamic evolution of the 2021 La Palma eruption. Nat. Commun. 14, 358. https://doi.org/10.1038/s41467-023-35953-y

Del Fresno, C., Cesca, S., Klügel, A., Domínguez Cerdeña, I., Díaz-Suárez, E.A., Dahm, T., García-Cañada, L., Meletlidis, S., Milkereit, C., Valenzuela-Malebrán, C., López-Díaz, R., López, C., 2023b. Magmatic plumbing and dynamic evolution of the 2021 La Palma eruption. Nat. Commun. 14, 358. https://doi.org/10.1038/s41467-023-35953-y

Devine, J.D., Gardner, J.E., Brack, H.P., Layne, G.D., Rutherford, M.J., 1995. Comparison of microanalytical methods for estimating H_2O contents of silicic volcanic glasses. Am. Mineral. 80, 319–328. https://doi.org/10.2138/am-1995-3-413

Di Carlo, I., Pichavant, M., Rotolo, S.G., Scaillet, B., 2006. Experimental Crystallization of a High-K Arc Basalt: the Golden Pumice, Stromboli Volcano (Italy). J. Petrol. 47, 1317–1343. https://doi.org/10.1093/petrology/egl011

Erdmann, S., Pichavant, M., Gaillard, F., 2024. Mineral-melt vanadium oxybarometry for primitive arc magmas: effect of hydrous melt composition on fO2 estimates. Contrib. Mineral. Petrol. 179, 39. https://doi.org/10.1007/s00410-024-02113-4

Froese, E., Gunter, A.E., 1976. A note on the pyrrhotite-sulfur vapor equilibrium. Econ. Geol. 71, 1589–1594. https://doi.org/10.2113/gsecongeo.71.8.1589

González, F., Seas, C., Barrientos, Z., Quesada-Acuña, S.G., Mora Amador, R.A., 2019. Poás Volcano Biodiversity, in: Tassi, F., Vaselli, O., Mora Amador, Raul Alberto (Eds.), Poás Volcano: The Pulsing Heart of Central America Volcanic Zone, Active Volcanoes of the World. Springer International Publishing, Cham, pp. 309–317. https://doi.org/10.1007/978-3-319-02156-0_13

González-García, D., Boulesteix, T., Klügel, A., Holtz, F., 2023. Bubble-enhanced basanite–tephrite mixing in the early stages of the Cumbre Vieja 2021 eruption, La Palma, Canary Islands. Sci. Rep. 13, 14839. https://doi.org/10.1038/s41598-023-41595-3

Hayer, C., Barrancos, J., Burton, M., Rodríguez, F., Esse, B., Hernández, P., Melián, G., Padrón, E., Asensio-Ramos, M., Pérez, N., 2022. From up above to down below: Comparison of satellite- and ground-based observations of SO2 emissions from the 2021 eruption of Cumbre Vieja, La Palma (other). display. https://doi.org/10.5194/egusphere-egu22-12201

Hughes, E.C., Saper, L.M., Liggins, P., O'Neill, H.S.C., Stolper, E.M., 2023. The sulfur solubility minimum and maximum in silicate melt. J. Geol. Soc. 180, jgs2021-125.

Jiménez-Mejías, M., Andújar, J., Scaillet, B., Casillas, R., 2021. Experimental determination of H 2 O and CO 2 solubilities of mafic alkaline magmas from Canary Islands. Comptes Rendus Géoscience 353, 289–314. https://doi.org/10.5802/crgeos.84

Jugo, P.J., 2004. An Experimental Study of the Sulfur Content in Basaltic Melts Saturated with Immiscible Sulfide or Sulfate Liquids at 1300 C and 1{middle dot}0 GPa. J. Petrol. 46, 783–798. https://doi.org/10.1093/petrology/egh097

Jugo, P.J., Luth, R.W., Richards, J.P., 2005. Experimental data on the speciation of sulfur as a function of oxygen fugacity in basaltic melts. Geochim. Cosmochim. Acta 69, 497–503. https://doi.org/10.1016/j.gca.2004.07.011

Keppler, H., 1999. Experimental Evidence for the Source of Excess Sulfur in Explosive Volcanic Eruptions. Science 284, 1652–1654. https://doi.org/10.1126/science.284.5420.1652

Lesne, P., Scaillet, B., Pichavant, M., 2015. The solubility of sulfur in hydrous basaltic melts. Chem. Geol. 418, 104–116. https://doi.org/10.1016/j.chemgeo.2015.03.025

Liu, Y., Samaha, N.-T., Baker, D.R., 2007. Sulfur concentration at sulfide saturation (SCSS) in magmatic silicate melts. Geochim. Cosmochim. Acta 71, 1783–1799. https://doi.org/10.1016/j.gca.2007.01.004

Lo Forte, F.M., Schiavi, F., Rose-Koga, E.F., Rotolo, S.G., Verdier-Paoletti, M., Aiuppa, A., Zanon, V., 2024. High CO2 in the mantle source of ocean island basanites. Geochim. Cosmochim. Acta 368, 93–111. https://doi.org/10.1016/j.gca.2024.01.016

Luhr, J.F., 1990. Experimental Phase Relations of Water- and Sulfur-Saturated Arc Magmas and the 1982 Eruptions of El Chich n Volcano. J. Petrol. 31, 1071–1114. https://doi.org/10.1093/petrology/31.5.1071

Moretti, R., Ottonello, G., 2005. Solubility and speciation of sulfur in silicate melts: The Conjugated Toop-Samis-Flood-Grjotheim (CTSFG) model. Geochim. Cosmochim. Acta 69, 801–823. https://doi.org/10.1016/j.gca.2004.09.006

Moune, S., Holtz, F., Botcharnikov, R.E., 2009. Sulphur solubility in andesitic to basaltic melts: implications for Hekla volcano. Contrib. Mineral. Petrol. 157, 691–707. https://doi.org/10.1007/s00410-008-0359-0

Moussallam, Y., Edmonds, M., Scaillet, B., Peters, N., Gennaro, E., Sides, I., Oppenheimer, C., 2016. The impact of degassing on the oxidation state of basaltic magmas: A case study of Kīlauea volcano. Earth Planet. Sci. Lett. 450, 317–325. https://doi.org/10.1016/j.epsl.2016.06.031

O'Neill, H.St.C., 2021. The Thermodynamic Controls on Sulfide Saturation in Silicate Melts with Application to Ocean Floor Basalts, in: Moretti, R., Neuville, D.R. (Eds.), Geophysical Monograph Series. Wiley, pp. 177–213. https://doi.org/10.1002/9781119473206.ch10

Oppenheimer, C., Fischer, T.P., Scaillet, B., 2014. Volcanic Degassing: Process and Impact, in: Treatise on Geochemistry. Elsevier, pp. 111–179. https://doi.org/10.1016/B978-0-08-095975-7.00304-1

Pérez, I.C., 2022. Relative velocity variations curves. https://doi.org/10.5281/ZENODO.6678861

Sandoval-Velasquez, A., Rizzo, A.L., Casetta, F., Ntaflos, T., Aiuppa, A., Alonso, M., Padrón, E., Pankhurst, M.J., Mundl-Petermeier, A., Zanon, V., Pérez, N.M., 2023. The noble gas signature of the 2021 Tajogaite eruption (La Palma, Canary Islands). J. Volcanol. Geotherm. Res. 443, 107928. https://doi.org/10.1016/j.jvolgeores.2023.107928

Scaillet, B., Clemente, B., Evans, B.W., Pichavant, M., 1998. Redox control of sulfur degassing in silicic magmas. J. Geophys. Res. Solid Earth 103, 23937–23949. https://doi.org/10.1029/98JB02301

Scaillet, B., Evans, B.W., 1999. The 15 June 1991 Eruption of Mount Pinatubo. I. Phase Equilibria and Pre-eruption P-T-fO2-fH2O Conditions of the Dacite Magma. J. Petrol. 40, 381–411. https://doi.org/10.1093/petroj/40.3.381

Scaillet, B., Luhr, J., Carroll, M.R., 2003. Petrological and volcanological constraints on volcanic sulfur emissions to the atmosphere. Geophys. Monogr.-Am. Geophys. Union 139, 11–40.

Scaillet, B., Pichavant, M., Roux, J., Humbert, G., Lefevre, A., 1992. Improvements of the Shaw membrane technique for measurement and control of fH2 at high temperatures and pressures. Am. Mineral. 77, 647–655.

Sisson, T.W., Grove, T.L., 1993. Experimental investigations of the role of H2O in calc-alkaline differentiation and subduction zone magmatism. Contrib. Mineral. Petrol. 113, 143–166. https://doi.org/10.1007/BF00283225

Taylor, J.R., Wall, V.J., Pownceby, M.I., 1992. The calibration and application of accurate redox sensors. Am. Mineral. 77, 284–295.

Ubide, T., Márquez, Á., Ancochea, E., Huertas, M.J., Herrera, R., Coello-Bravo, J.J., Sanz-Mangas, D., Mulder, J., MacDonald, A., Galindo, I., 2023. Discrete magma injections drive the 2021 La Palma eruption. Sci. Adv. 9, eadg4813. https://doi.org/10.1126/sciadv.adg4813

Whitney, J.A., 1984. Fugacities of sulfurous gases in pyrrhotite-bearing silicic magmas. Am. Mineral. 69, 68–78.

Zanon, V., D'Auria, L., Schiavi, F., Cyrzan, K., Pankhurst, M.J., 2024. Toward a near real-time magma ascent monitoring by combined fluid inclusion barometry and ongoing seismicity. Sci. Adv. 10, eadi4300. https://doi.org/10.1126/sciadv.adi4300

616